H2O–CO2 solubility in low SiO2-melts and the unique mode of kimberlite degassing and emplacement

Yves Moussallam, Yann Morizet, Fabrice Gaillard

H_2O-CO_2 Solubility in low SiO_2-melts and the unique mode of kimberlite degassing and emplacement

Yves Moussallam[1], Yann Morizet[2,3], Fabrice Gaillard[2]

[1] *Geosciences Research Division, Scripps Institution of Oceanography, UCSD, La Jolla, California 92093-0244, USA*

[2] *ISTO, 7327 Université d'Orléans-CNRS-BRGM, 1A rue de la Férollerie, 45071 Orléans cedex 2, France*

[3] *Université de Nantes, Nantes Atlantique Universités, Laboratoire de Planétologie et Géodynamique de Nantes (LPGN) UMR CNRS 6112*

Corresponding author: Yves Moussallam; ymoussallam@ucsd.edu

ABSTRACT

Kimberlites are the most deep-seated magmas in the mantle and ascend to the surface at an impressive speed, travelling hundreds of kilometres in just hours while carrying a substantial load of xenolithic material, including diamonds. The ascent dynamics of these melts are buoyancy-controlled and certainly driven by outgassing of volatile species, presumably H_2O and CO_2, summing to concentration level of ca 15 – 30 wt.% in kimberlite melts. We provide H_2O-CO_2 solubility data obtained on quenched glasses that are synthetic analogues of kimberlite melts (SiO_2 content ranging from 18 to 28 wt%). The experiments were conducted in the pressure range 100 to 350 MPa. While the CO_2 solubility can reach 20 wt%, we show that the H_2O solubility in these low silica melts is indistinguishable from that found for basalts. Moreover, whereas in typical basalts most of the water exsolves at shallower pressure than the CO_2, the opposite relationship is true for the low-SiO_2 composition investigated. These data show that kimberlites can rise to depths of the upper crust without suffering significant degassing and must release large quantities of volatiles (>15 wt.%) within the very last few kilometres of ascent. This unconventional degassing path may explain the

characteristic pipe, widening-upward from a ≤ 2.5 km deep root zone, where kimberlites are mined for diamonds. Furthermore, we show that small changes in melt chemistry and original volatile composition (H_2O vs CO_2) provide a single mechanism to explain the variety of morphologies of kimberlite pipes found over the world. The cooling associated to such massive degassing must freeze a large quantity of melt explaining the occurrence of hypabyssal kimberlite. Finally, we provide strong constraints on the primary volatile content of kimberlite, showing that the water content reported for kimberlite magma is mostly reflective of secondary alteration.

HIGHLIGHTS

- Determination of H_2O solubility in very low-SiO_2 melts
- The water content reported for most natural kimberlite cannot be primary
- The original H_2O vs CO_2 content of kimberlite melts defines the depth of pipe root zone

1. INTRODUCTION

Kimberlite occur as shallow bowl-shaped bodies or steep sided (60° to ~90°) craters and pipes, hundreds of metres in diameter at most, extending vertically to depth of 0.5 to 2.5 km. Pipes display a widening upward structure initiating at the root zone and terminating at the crater (Scott Smith, 2008; Smith et al., 2013). The variety in the depth extent of kimberlite pipes and root zones, together with petrologic differences, has prompted their organisation into three classes (Field and Scott Smith, 1998; Scott Smith, 2008). Class 1 represent the classical deep, steep sided pipes mostly recognised from studies of South African occurrences. Class 2 and 3 are smaller and mostly recognised from Canadian occurrences;

class 2 show much shallower to almost non-existent pipes and root zones while class 3 have pipes infilled predominantly with re-sedimented volcaniclastic material (Field and Scott Smith, 1998).

The origin of kimberlite pipes was originally envisioned as the result of degassing of large quantities of magmatic volatiles (H_2O and dominantly CO_2) accompanied by important volume change and fluidization at a pressure of ~80 MPa (depth of ~2.6 km) (Dawson, 1971). The realisation, however, that not all kimberlite pipes feature such deep root zones, suggests this theory is incomplete as it is unable to explain why magmatic volatile exsolution would not occur at a fixed pressure. The principal alternative model involves magma – groundwater interaction. This model has gained popularity (Lorenz, 1975; Skinner and Marsh, 2004; Kjarsgaard, 2007; Kurszlaukis and Lorenz, 2008) but remains unable to explain the entire range of pipe morphologies, depth extent and evidence of magmatic pyroclasts (Scott Smith, 2008).

In this study we present results from the first mix H_2O-CO_2 solubility experiments in transitional melts (melts of composition intermediate between a silicate and a carbonate liquid). We corroborate and expand findings from CO_2 solubility experiments on similar compositions (Moussallam et al., 2014), showing that the solubility of CO_2 in transitional melts has a highly non-linear relationship to pressure, dissimilar to its relation in both silicate and carbonate melts. We show, in contrast, that the solubility of H_2O in transitional melts is similar to H_2O solubility determined in classical silicate melt compositions such as basalt. By combining CO_2 and H_2O solubility laws we then calculate the closed system degassing of an ascending transitional melt. We show that small changes in the melt silica and most importantly water content, can dramatically affect the depth at which CO_2 is released from

kimberlitic melts controlling the emplacement dynamics. We suggest that a variety of small changes in the melt chemical composition, including changes in the water content can successfully explain the variety of kimberlite pipe depth extent. Water-rich kimberlites produce strong CO_2 outgassing at high pressure, resulting in pipes with deep root zones (typical of Class 1 African kimberlites; Field and Scott Smith, 1998) whereas water-poor kimberlites retain their CO_2 up to lower pressures, producing shallow root zones (typical of Class 2 Canadian kimberlites) and promoting possible interaction with groundwater. While kimberlite pipes exhibit a great diversity of morphologies, their eruption process need not be dissimilar.

2. METHODS

2.1 Pertinence of the investigated composition

The high number of external materials carried by the ascending magma (xenocrysts and xenolith, including those containing diamonds (Kelley and Wartho, 2000; Mitchell, 2008; Walter et al., 2011; Russell et al., 2012) and the chaotic emplacement dynamics make the recovery of primary kimberlite melt compositions difficult. As a result, the original composition of natural kimberlite is unknown and highly debated (e.g., Sparks, 2013). Close-to-primary magmatic composition were believed to be preserved in rare occurrences of aphanitic kimberlite as found in South Africa (e.g., Becker and Roex, 2006) and Canada (Price et al., 2000) but even those have been shown to contain a large proportion of lithospheric olivine and distinguishing xenocrystic to phenocrystic olivine has proved a challenging endeavour (Arndt et al., 2006, 2010; Kamenetsky et al., 2008; Brett et al., 2009, 2015). While estimates of primary kimberlite composition vary widely, most recent studies (Harris et al., 2004; Kopylova et al., 2007) point to a melt with very low silica content (18 to

30 wt% SiO_2) and high alkaline-earth content (30-45 wt.% MgO + CaO) that shows many similitude with carbonatites (e.g., Russell et al., 2013; Kamenetsky et al., 2014; Brett et al., 2015). Such melt compositions are clearly outside the calibration range of common models of volatile solubility in silicate melts (Papale et al., 2006; Iacono-Marziano et al., 2012) and experimental investigations approaching these (low-silica) compositions have remained scarce (Brey and Ryabchikov, 1994; Brooker et al., 2011) due to experimental difficulties especially at low pressure (<500 MPa) relevant to the emplacement depth of kimberlite pipes. Kimberlite magmas are depolymerized in nature (NBO/T > 3; where NBO/T represents the amount of Non-Bridging Oxygen per tetrahedral calculated from the chemical composition stoichiometry) and as such have a strong capability to accommodate large quantities of volatiles (Brooker et al., 2001a; Iacono-Marziano et al., 2012). Here, we have prepared synthetic melts with the following properties (i) low SiO_2 content (25 to 32 wt% SiO_2 on a volatile-free basis; Table 1) (ii) high alkaline-earth content (53 to 63 wt% MgO + CaO on a volatile-free basis) and (iii) highly depolymerise configuration (calculated NBO/T > 3) with the aim of capturing the critical characteristics of kimberlite melts and addressing the compositional complexity of natural silicate-carbonated liquids while retaining the ability to quench to pure glass under experimental conditions (Moussallam et al., 2014) using a special setting in the experimental apparatus allowing very fast isobaric quench rate.

2.2 Starting material

Starting materials were produced by mixing powders from a natural lamproite from Torre Alfina, Italy (Iacono-Marziano et al., 2012; fused twice at 1400°C) with various amounts of synthetic powders of pure oxides and natural dolomite $(Ca,Mg)CO_3$. The composition of all mixtures used as starting materials of all experiments is reported in Table 1. The investigated compositions cover the range from 25 to 32 wt% SiO_2 on a volatile-free basis.

All experiments were performed in internally heated pressure vessels operating vertically and loaded with Ar as the pressurizing medium and at oxygen fugacity conditions of logfO_2= FMQ+3. Experimental charges consisted of anhydrous sample powder (100 to 150 mg) loaded in gold-palladium ($Au_{80}Pd_{20}$) capsules (3-4 cm in length, 2.5 mm inner diameter and 2.9 mm outer diameter) with variable amounts of water (added as pure H_2O). The capsules were welded shut using a PUK 3 arc welder in micro mode, ensuring no heating of the capsule and no loss of water. The water and powder mix were homogenised for 48h at 140°C. For each experiment, one single capsule was hanged by a thin Pt wire. Rapid quenching was achieved by passing an electrical current to the holding Pt wire so that the sample dropped into the cold, bottom part of the furnace. The cooling rate was estimated to >400°C s^{-1} although no precise estimate could be obtained.

After each experiment, capsules were weighed (i) directly after each experimental run (ii) after piercing and (iii) after heating at 140°C for an hour to ensure all water had evaporated and to determine the total amount of gas not incorporated in the glass. Capsules were then opened and a fragment of the charge was embedded in an epoxy resin and polished for SEM and microprobe analyses. We conducted a total of 14 H_2O-CO_2 solubility experiments using two melt compositions having SiO_2 content of 25 and 32 wt.% (on a volatile-free basis). All experiments successfully produced a clear glass. All experimental products were examined by optical microscope and scanning electronic microscope (SEM) to check for the presence of quench crystals.

We used a Thermo Scientific, Flash 2000, CHNS elemental analyser to measure water (as H) and CO_2 (as C) in all experimental products. About 1 mg of sample was loaded in a tin

capsule folded and analysed by combustion at 1800°C. The analyser was calibrated directly prior to analysis and reproducibility on external standards (marble, dolomite and hydrated basalt) was found to be better than 2% for C and 10% for H, samples replicate ran over several sessions (i.e. several calibration lines) yield a conservative estimated error (one standard deviation) of 10% in relative on CO_2 measurement and 20% on H_2O measurements.

Electron microprobe analyses (EMPA) were performed on a Cameca SXFive at the ISTO-CNRS laboratory in Orléans. Glasses were analysed using an accelerating voltage of 15 kV, a beam current of 6 nA and a defocused beam of 10 µm. Na and K were analysed first in order to minimise alkali loss during analysis. The shortfall in the totals for analysed glasses was broadly consistent with the H_2O + CO_2 content estimated by elemental analyser, but systematically higher.

3. RESULTS

3.1 Evidence of glassy state

In this section we show that (i) experiments produced clear glass, free of any quench crystals and (ii) that carbon in the glass is present as carbonate ions (CO_3^{2-}). Fig. 1 shows optical microphotograph of recovered glasses. It can be seen that high pressure synthesised glasses are optically clear, attesting for the absence of quench crystals. An average of twenty electron microprobe analyses on each glass is presented in Table 2, the very low standard deviations on major elements analyses (Table S1) further attest of the glass homogeneity. The absence of quench crystals is also confirmed from the smooth infrared and Raman spectra (Fig. 2) which also show that CO_2 is dissolved as carbonate ions (CO_3^{2-}) in the glass. No evidence for CO_2^{mol} was observed in the Raman spectra at ~1400 cm^{-1} nor in the FTIR spectra at 2350 cm^{-}

[1] (Brooker et al., 1999). This observation is consistent with our current knowledge on the CO_2 dissolution mechanisms as a function of silicate melt composition: CO_2^{mol} being solely present in Si-rich glass composition such as rhyolite (Brooker et al., 1999; Tamic et al., 2001) and totally absent for Si-poor glass compositions (Brooker et al., 2001b; Morizet et al., 2014). The presence of water in the glass is illustrated in both the infrared and Raman spectra by the H_2O + OH band at 3550 cm^{-1}. The speciation of water in the glass was not resolved.

3.2 H_2O-CO_2 Solubility

Results from a series of H_2O-CO_2 fluid-saturated, supra-liquidus experiments for two transitional melt compositions (25 and 32 wt% SiO_2 on a volatile-free basis) equilibrated at a range of pressure from 100 to 350 MPa are shown in Fig. 3. Our results indicate that CO_2 solubility behaviour in low-silica melts is extremely dissimilar to that in common silicate melts (i.e. MORB). At equal pressure the solubility of CO_2 is up to two orders of magnitude greater in kimberlite melt than in a typical basalt. Whereas the solubility of CO_2 increases nearly linearly with pressure in a basaltic melt over this pressure range (e.g., Dixon, 1997; Shishkina et al., 2010) , the increase in CO_2 content is nearly exponential in a kimberlitic melt (as described by the model of Moussallam et al., (2014) for equilibrium with a pure CO_2 fluid). In contrast, our results indicate that the solubility of H_2O in kimberlite is nearly identical to that found in common silicate melts such as MORB and drastically different to that in carbonatite (where ~10wt% H_2O can be dissolved at 100 MPa; Keppler, 2003). Indeed our results do not deviate significantly from a power law relationship to f_{H2O} typical for basaltic melts (Shishkina et al., 2010). Unexpectedly, at a given pressure, equal amount of water can be dissolved in a kimberlite and in a basalt (Fig. 3). While these findings do not directly inform us on the primary volatile content of kimberlites, they do unequivocally

constrain the maximum amount of H_2O and CO_2 that can be dissolved in kimberlite melts as a function of pressure.

4. DISCUSSION

4.1 Novelty of determined solubility behaviour

In this section we compare the H_2O-CO_2 solubility laws obtained in this study with current thermodynamic models from the literature to emphasise the importance of these new measurments. We start by investigating the widely used model of Papale et al., (2006) for two-component H_2O + CO_2 fluid in silicate liquids and compare the model prediction with our measurements (for a composition containing 25 wt.% SiO_2 on a volatile free basis; Fig. 4). The model of Papale et al., (2006) predicts a solubility of up to 16 wt.% H_2O at 350 MPa (for pure H_2O fluid) and up to 13 wt.% CO_2 (for pure CO_2 fluid) as compared to the ~ 8 wt.% H_2O and ~ 20 wt.% CO_2 we obtained for similar conditions. Furthermore, the general shape of the H_2O-CO_2 dependency obtained with the model of Papale et al., (2006) is markedly different from the one we derive from the actual measurements. For a given X_{H2O} in the fluid phase the model consistently predicts a much higher water content than measured (e.g., at X_{H2O} = 0.4 the model predicts a solubility of ~ 7 wt.% H_2O compared to the ~ 3 wt.% measured and a solubility of ~ 4 wt.% CO_2 compared to the ~ 18 wt.% measured). Other published H_2O-CO_2 solubility models such as VOLATILECALC (Newman and Lowenstern, 2002) and the model of Iacono-Marziano et al. (2012) cannot perform calculations on such low SiO_2 melts.

The model of kimberlite ascent of Russell et al., (2012) was based on experiments performed at one atmosphere and did not provide any data on the pressure dependence of CO_2 solubility. A thorough dynamical model of melt ascent was performed by Sparks et al., (2006) who

assumed a solubility behaviour for CO_2 similar to basaltic melt (i.e. linear dependence on pressure, Fig. 4) starting with 20 wt.% CO_2 dissolved at 200 km depth. In addition, their model did not consider water. We stress that the solubility data we present here are the very first to consider two-component H_2O + CO_2 fluid in kimberlite-type melts. Our results show strikingly different volatile behaviour than all models considered by previous workers.

4.2 Water content of natural kimberlite

Fig. 3c shows that the vast majority of measured volatile contents of "uncontaminated" kimberlite samples (database from Kjarsgaard et al., 2009) are at odd with the pressures associated with root zone depths of up to a few kilometres (<100 MPa). According to our experimental results, the measured water contents of natural kimberlite, reaching as high as 14 wt.% cannot be the original water content of the kimberlitic melt at the time of emplacement. The observed H_2O content would require pressures > 1500 MPa, equivalent to emplacement depth exceeding 50 km. We strongly argue that the very high water content (>9-10 wt.% H_2O) reported for kimberlite melts must be secondary, most probably associated with serpentinization. Serpentinization will not only affect the water content of a kimberlite rock but can also increase its SiO_2 and MgO content (exact reaction depending on the fluid composition; e.g., Stripp et al., 2006). This is consistent with Mg number reported in kimberlite being typically too high for equilibrium with a mantle sources (Price et al., 2000; Kopylova et al., 2007) although this feature may partially be explained by orthopyroxene assimilation (e.g., Russell et al., 2012).

4.3 Modelling kimberlite close-system degassing

We have modelled the consequences of the pressure-dependence of the mixed H_2O-CO_2 volatile behaviour in the investigated haplo-kimberlite analogue compositions. We used the

determined solubility laws to parameterise a code solving the gas-melt equilibria in the C–H–O system as a function of pressure (described in Gaillard et al., 2011). The CO_2 solubility model used here is the empirical model of Moussallam et al., (2014) (shown in Fig 3b) which is calibrated on experiments for CO_2 dissolved in SiO_2-poor melt compositions that were successfully quenched to glass. These glasses tend to be Ca-rich but the model does reproduce more Mg-rich experimental data such as those of Brey and Ryabchikov, (1994) (see Fig. 5 in Moussallam et al., 2014). Increasing the Mg/Ca ratio should induce a decrease in CO_2 solubility but while this decrease may be important in common silicate melt such as basalts (Dixon, 1997), the effect in low SiO_2 melts remains to be resolved. The absolute CO_2 solubility obtained from the model used in this study may be considered as maximum values for natural, more Mg-rich kimberlites. The evolution of the solubility profile with respect to pressure (i.e. strongly non-linear) however, should hold regardless of the exact melt composition. With respect to water, our results clearly show that there is very little effect of composition on the solubility of water over the investigated SiO_2 content (Fig. 3a). The solubility law used here (shown in Fig. 3a, power law relationship between the amount of water dissolved in the melt and f_{H2O}) is therefore applicable to natural kimberlite melt regardless of their exact composition.

Fig. 5 shows, for two different starting compositions (SiO_2 of 25 and 32 wt.% on a volatile-free basis) the effect of H_2O on the solubility of CO_2 in kimberlite. The two starting compositions were chosen in order to bracket the range of possible composition (in term of SiO_2 + Al_2O_3 content) at which a kimberlite reaches the lower crust. From the thermodynamic standpoint, the effect of dissolved water is essentially to lower the f_{CO2} (the fugacity of CO_2 in the fluid phase, i.e. the CO_2 activity) at a given pressure, hence forcing CO_2 exsolution from the melt. The addition of H_2O also modifies the shape of the CO_2

solubility vs pressure relationship making it slightly less exponential and more linear. We stress that these effects would also hold for more Mg-rich melt compositions.

4.4 Modelling kimberlite ascent

The strong control of H_2O on CO_2 solubility in kimberlite will strongly affect their ascent dynamics. To explore this effect we coupled the chemical solubility model with a physical model of magma ascent as a closed system in a self-propagating dyke based on previous models (Lister and Kerr, 1991; Sparks et al., 2006). The model is based on a number of assumptions and simple constraints:

(i) The melt rises as a close system; no CO_2 escape, no crystal settling.

(ii) The melt density is calculated as:

$$\rho = \sum_{i=1}^{N} \frac{X_i M_i}{V_i} \quad (1)$$

Where ρ is the melt density (in kg m^{-3}), N is the total number of oxides in the melt, X_i is the mole fraction of the i^{th} oxide (dimensionless), M_i is the molecular weight of the i^{th} oxide (in kg mol^{-1}) and V_i is the fractional volume of the i^{th} oxide (in m^3 mol^{-1}).

Partial molar volumes (used to calculate to the fractional volume) for SiO_2, Al_2O_3, MgO, CaO, Na_2O, K_2O and H_2O are calculated following the model of Ochs and Lange, (1997):

$$\bar{V}_i = \bar{V}_{i,T_{ref}} + \left(\frac{d\bar{V}_i}{dT}\right)(T - T_{ref}) + \left[\left(\frac{d\bar{V}_i}{dP}\right)_{T_{ref}} + \frac{\left(\frac{d\bar{V}_i}{dP}\right)}{dT}(T - T_{ref})\right](P - P_{ref})$$

Partial molar volumes for TiO_2 and FeO are taken from Bottinga and Weill, (1970) and for CO_2 from Seifert et al., (2013) (using value determined for basaltic

melt), CO_2 densities at high pressure are taken from Bottinga and Richet, (1981), H_2O densities at high pressure are taken from the NIST database for H_2O.

(iii) Melt viscosity is assumed to remain constant at 0.3 Pa s.

(iv) The crust is modelled with a mean density of 2.8 g/cm^3.

(v) The effect of temperature changes due to adiabatic cooling (i.e. Kavanagh and Sparks, 2009) and resulting crystallisation of the kimberlite melt are not considered.

(vi) Ascent rates were constrained by the equation from Lister and Kerr, (1991) as used by Sparks et al., (2006), describing the propagation of a fluid filled fracture under turbulent conditions, assuming a constant dyke width of 1 meter:

$$u = 7.7[w^5/\{\mu^3(\rho g \Delta\rho)\}]^{1/7} g\Delta\rho \qquad (2)$$

Where u is the ascent velocity (in m s^{-1}), 7.7 is an experimentally determined factor, w is the width of the dyke (in m), μ is the viscosity (in Pa s), ρ is the magma density (in kg m^{-3}) and Δρ is the density difference between the kimberlite magma and the surrounding crust.

We note that several aspect of this model are intentionally close to that of Sparks et al., (2006) notably with regard to the choice of constant parameters (viscosity of 0.3 Pa s^{-1} and dike width of 1 m). The volatile solubility laws however - driving the ascent - are notably different.

The result of ascent scenarios for two melt compositions (SiO_2 of 23 and 29 wt.% on a volatile-free basis) starting with variable amount of water (and at CO_2 saturation) are reported in Fig. 5. The results show that ascending water–rich kimberlites will exsolve higher amount of volatiles (mostly CO_2), sooner (at greater depth) than their water–poor counterparts hence reaching the last few kilometres of crust (depth characteristic of the deepest root zones) with

a lower volatile content than H_2O-free melts. The effect on ascent dynamics is that a water-rich kimberlite dyke will rise faster (travelling 50 km of crust in ~20 min) and accelerate at greater depth than a H_2O-free melts. This ascent is propelled by an increased in the volume fraction of exsolved gas causing the magma density to be reduced by a third at 3.5 – 4.5 km from the surface in H_2O-free melts and at 7 – 8.5 km from the surface in H_2O-rich melts. All melts considered will travel the last 2.5 kilometres of the crust in less than ~30 sec. The range of volatile (H_2O + CO_2) content at which a kimberlite will enter these last 2.5 km, varies from 16 to 8 wt.% while original volatile contents explored ranged from 25 to 35 wt.%. Additional ascent scenarios exploring the effect of starting conditions are reported in the Supplementary Information. These additional scenarios show a very week effect of the model starting pressure and that changing melt viscosity, xenolithic content and dyke width only result in translating the absolute ascent velocity without impacting the shape of the ascent velocity profile.

4.5 Implications for kimberlite volcanism and kimberlite pipe formation

All ascent scenarios predict the release of large amounts of volatiles, 30 to 70% of the initial load, in the last few kilometres of crust. This huge release of gas will be associated with a large volume increase over a very short time increment, fracturing the country rock and generating a widening upward kimberlite pipe. In detail, the results show that ascending water–rich kimberlites will exsolve higher amount of CO_2, sooner (at greater depth) than their water–poor counterparts hence reaching the last few kilometres of crust (depth characteristic of the deepest root zones) with a lower volatile content than H_2O-free melts. The increasing volume fraction of gas will enhance the magma buoyancy and rise speed and when reaching the critical value of ~70 to 80%, the phase will change from a bubbly liquid magma to an ash-laden gas (e.g., Woods, 1995). This will result in an even stronger ascent rate than

currently modelled and be associated with a large volume increase. For these reasons it is taken here as the estimated starting point of pipe formation. As shown in Fig. 6, the depth at which catastrophic volatile release, phase change and pipe initiation takes place is hence a strong function of the melt chemistry, in particular of the original water vs CO_2 content. The depth of pipe initiation varies in our ascent scenarios from ~2.6 to 1.1 km, reproducing most of the natural range of kimberlite root zone (2.5 to 0.5 km). Water-rich compositions reach the critical value and initiate pipe formation at greatest depth (Fig. 6). H_2O-poor and silica-poor compositions can ascend to shallower depth and therefore have greater chance of interacting with groundwater and initiate phreatomagmatic emplacement processes. In nature, the infill in Class 1 pipes with deep root zones is completely devoid of primary carbonate and contains abundant serpentine whereas in Class 2 pipes, with shallower root zone, primary magmatic or deuteric carbonate is abundant as infill while serpentine is less abundant (Smith et al., 2013). This mineralogical difference hints, as previously suggested (Skinner and Marsh, 2004), to Class 1 kimberlite being comparatively water-rich as compared to more CO_2-rich Class 2 kimberlite.

The sudden loss of volatile will strongly increase the melt liquidus temperature and decrease the temperature of the system since H_2O-CO_2 volatilization and decompression are endothermic processes (Russell, 1987). This instant degassing must therefore lead to sudden crystallisation of the melt and stalling of the kimberlite ascent at depth. Such scenario could explain the formation of kimberlite sills and dike recognised as hypabyssal kimberlite and occurring at a similar depth level than diatremes. Whether an ascending kimberlite stall or erupt upon losing its volatile will primarily depend on the capacity of the gas phase to decouple from the liquid. Close system degassing will lead to fragmentation and pipe

initiation while open system degassing (in which the gas ascends faster and separates from the liquid) will lead to a crystallising and stalling hypabyssal kimberlite.

We suggest that kimberlite pipes with deep root zones results from the ascent of water-rich and possibly more silica-rich melts than kimberlite pipes exhibiting shallower root zone. We further propose that the current class 1 and class 2 kimberlite classification may represent end-members from a continuum in eruptive style, dictated by the original melt composition and volatile content. Class 3 kimberlites might be hybrids between these end-members or alternatively represent water-rich kimberlites with a different SiO_2+Al_2O_3 content and hence very different amount of volatiles but still exsolving at depth.

Kimberlite melts are generated by very low degree partial melting of the mantle. Their composition is highly dependent on the temperature, the degree of melting (Dalton and Presnall, 1998) but also on the original volatile content of the mantle (H_2O and CO_2) (Dasgupta et al., 2013). The apparent correlation between kimberlite classes and geographic location (Field and Scott Smith, 1998) might reflect contrasting mantle thermal profile or mantle volatile content since both high temperature and high water or carbon content in the mantle increases the equilibrium silica content of kimberlite melts and deepens their root zone.

5. CONCLUSION

We have investigated the solubility of mixed H_2O-CO_2 volatiles in kimberlite melts using experiments performed on silica-poor synthetic compositions as analogues for primary kimberlite melts. We have modelled the effect of the mixed volatile solubility behaviour on

the close system degassing and ascent dynamics of kimberlites. The key conclusions we draw from our findings are:

i. The solubility of H_2O in kimberlite melts is similar to that in common silicate melts, following a power-law relationship to f_{H2O}.

ii. The water content reported for most natural kimberlite cannot be primary but is mostly reflective of secondary alteration.

iii. Kimberlite melts can retain most of their volatile load up until the last few kilometres of ascent at which point a massive release of volatiles occurs initiating pipe formation.

iv. The exact depth at which this catastrophic release occurs is function of the initial volatile (CO_2 vs H_2O) and melt composition. Water-rich (and silica-rich) kimberlite are predicted to initiate pipe formation at greater depth than comparatively CO_2-rich (or water-poor) (and silica-poor) kimberlite. This provides a single mechanism to explain the variations in shape and vertical extents of kimberlite pipes worldwide.

ACKNOWLEDGEMENTS

We are very grateful to Rémi Champallier for his help with various instruments. Special thanks also go to Ida Di Carlo for help with the electron probe analyses and to Marielle Hatton for help with the elemental analyser. This work was supported by the European Research Council (ERC grant number 279790) and the French agency for research (ANR project #2010 BLAN62101). Valuable comments by two anonymous reviewers improved the quality of the manuscript.

REFERENCES

Arndt, N. T., Boullier, A. M., Clement, J. P., Dubois, M., Schissel, D., 2006. What olivine, the neglected mineral, tells us about kimberlite petrogenesis. EEarth Discuss. 1, 37–50.

Arndt, N. T., Guitreau, M., Boullier, A.-M., Roex, A. L., Tommasi, A., Cordier, P., Sobolev, A., 2010. Olivine, and the Origin of Kimberlite. J. Petrol. 51, 573–602.

Becker, M., Roex, A. P. L., 2006. Geochemistry of South African On- and Off-craton, Group I and Group II Kimberlites: Petrogenesis and Source Region Evolution. J. Petrol. 47, 673–703.

Behrens, H., Misiti, V., Freda, C., Vetere, F., Botcharnikov, R. E., Scarlato, P., 2009. Solubility of H (sub 2) O and CO (sub 2) in ultrapotassic melts at 1200 and 1250 degrees C and pressure from 50 to 500 MPa. Am. Mineral. 94, 105–120.

Botcharnikov, R. E., Behrens, H., Holtz, F., 2006. Solubility and speciation of C–O–H fluids in andesitic melt at T = 1100–1300 °C and P = 200 and 500 MPa. Chem. Geol. 229, 125–143.

Bottinga, Y., Richet, P., 1981. High pressure and temperature equation of state and calculation of the thermodynamic properties of gaseous carbon dioxide. Am. J. Sci. 281, 615–660.

Bottinga, Y., Weill, D. F., 1970. Densities of liquid silicate systems calculated from partial molar volumes of oxide components. Am. J. Sci. 269, 169–182.

Brett, R. C., Russell, J. K., Andrews, G. D. M., Jones, T. J., 2015. The ascent of kimberlite: Insights from olivine. Earth Planet. Sci. Lett. 424, 119–131.

Brett, R. C., Russell, J. K., Moss, S., 2009. Origin of olivine in kimberlite: Phenocryst or impostor? Lithos 112, Supplement 1, 201–212.

Brey, G. ., Ryabchikov, I. ., 1994. Carbon dioxide in strongly undersaturated melts and origin of kimberlitic magmas. N Jb Min. Mh H10, 449–463.

Brooker, R. A., Kohn, S. C., Holloway, J. R., McMillan, P. F., 2001a. Structural controls on the solubility of CO2 in silicate melts: Part II: IR characteristics of carbonate groups in silicate glasses. Chem. Geol. 174, 241–254.

Brooker, R. A., Kohn, S. C., Holloway, J. R., McMillan, P. F., Carroll, M. R., 1999. Solubility, speciation and dissolution mechanisms for CO2 in melts on the NaAlO2–SiO2 join. Geochim. Cosmochim. Acta 63, 3549–3565.

Brooker, R. A., Sparks, R. S. J., Kavanagh, J. L., Field, M., 2011. The volatile content of hypabyssal kimberlite magmas: some constraints from experiments on natural rock compositions. Bull. Volcanol. 73, 959–981.

Brooker, R. ., Kohn, S. ., Holloway, J. ., McMillan, P. ., 2001b. Structural controls on the solubility of CO2 in silicate melts: Part I: bulk solubility data. Chem. Geol. 174, 225–239.

Dalton, J. A., Presnall, D. C., 1998. The Continuum of Primary Carbonatitic–Kimberlitic Melt Compositions in Equilibrium with Lherzolite: Data from the System CaO–MgO–Al2O3–SiO2–CO2 at 6 GPa. J. Petrol. 39, 1953–1964.

Dasgupta, R., Mallik, A., Tsuno, K., Withers, A. C., Hirth, G., Hirschmann, M. M., 2013. Carbon-dioxide-rich silicate melt in the Earth's upper mantle. Nature 493, 211–215.

Dawson, J. B., 1971. Advances in kimberlite geology. Earth-Sci. Rev. 7, 187–214.

Dixon, J. E., 1997. Degassing of alkalic basalts. Am. Mineral. 82, 368–378.

Field, M., Scott Smith, B. H., 1998. Contrasting Geology and Near-Surface Emplacement of Kimberlite Pipes in Southern Africa and Canada., in: . Red Roof Designs, Cape Town, South Africa,

Gaillard, F., Scaillet, B., Arndt, N. T., 2011. Atmospheric oxygenation caused by a change in volcanic degassing pressure. Nature 478, 229–232.

Harris, M., le Roex, A., Class, C., 2004. Geochemistry of the Uintjiesberg kimberlite, South Africa: petrogenesis of an off-craton, group I, kimberlite. Lithos 74, 149–165.

Iacono-Marziano, G., Morizet, Y., Le Trong, E., Gaillard, F., 2012. New experimental data and semi-empirical parameterization of H2O–CO2 solubility in mafic melts. Geochim. Cosmochim. Acta 97, 1–23.

Kamenetsky, V. S., Golovin, A. V., Maas, R., Giuliani, A., Kamenetsky, M. B., Weiss, Y., 2014. Towards a new model for kimberlite petrogenesis: Evidence from unaltered kimberlites and mantle minerals. Earth-Sci. Rev. 139, 145–167.

Kamenetsky, V. S., Kamenetsky, M. B., Sobolev, A. V., Golovin, A. V., Demouchy, S., Faure, K., Sharygin, V. V., Kuzmin, D. V., 2008. Olivine in the Udachnaya-East Kimberlite (Yakutia, Russia): Types, Compositions and Origins. J. Petrol. 49, 823–839.

Kavanagh, J. L., Sparks, R. S. J., 2009. Temperature changes in ascending kimberlite magma. Earth Planet. Sci. Lett. 286, 404–413.

Kelley, S. P., Wartho, J.-A., 2000. Rapid Kimberlite Ascent and the Significance of Ar-Ar Ages in Xenolith Phlogopites. Science 289, 609–611.

Keppler, H., 2003. Water solubility in carbonatite melts. Am. Mineral. 88, 1822–1824.

Kjarsgaard, B. A., 2007. Kimberlite pipe models; significance to exploration. Proc. - Decenn. Int. Conf. Miner. Explor. 5, 667–677.

Kjarsgaard, B. A., Pearson, D. G., Tappe, S., Nowell, G. M., Dowall, D. P., 2009. Geochemistry of hypabyssal kimberlites from Lac de Gras, Canada: Comparisons to a

global database and applications to the parent magma problem. Lithos 112, Supplement 1, 236–248.

Kopylova, M. G., Matveev, S., Raudsepp, M., 2007. Searching for parental kimberlite melt. Geochim. Cosmochim. Acta 71, 3616–3629.

Kurszlaukis, S., Lorenz, V., 2008. Formation of "Tuffisitic Kimberlites" by phreatomagmatic processes. J. Volcanol. Geotherm. Res. 174, 68–80.

Lister, J. R., Kerr, R. C., 1991. Fluid-mechanical models of crack propagation and their application to magma transport in dykes. J. Geophys. Res. Solid Earth 96, 10049.

Lorenz, V., 1975. Formation of phreatomagmatic maar-diatreme volcanoes and its relevance to kimberlite diatremes. Phys. Chem. Earth 9, 17–27.

Mitchell, R. H., 2008. Petrology of hypabyssal kimberlites: Relevance to primary magma compositions. J. Volcanol. Geotherm. Res. 174, 1–8.

Morizet, Y., Paris, M., Gaillard, F., Scaillet, B., 2014. Carbon dioxide in silica-undersaturated melt. Part I: The effect of mixed alkalis (K and Na) on CO2 solubility and speciation. Geochim. Cosmochim. Acta 141, 45–61.

Moussallam, Y., Morizet, Y., Massuyeau, M., Laumonier, M., Gaillard, F., 2014. CO2 solubility in kimberlite melts. Chem. Geol.

Newman, S., Lowenstern, J. B., 2002. VolatileCalc: a silicate melt–H2O–CO2 solution model written in Visual Basic for excel. Comput. Geosci. 28, 597–604.

Ochs, F. A., Lange, R. A., 1997. The partial molar volume, thermal expansivity, and compressibility of H2O in NaAlSi3O8 liquid: new measurements and an internally consistent model. Contrib. Mineral. Petrol. 129, 155–165.

Papale, P., Moretti, R., Barbato, D., 2006. The compositional dependence of the saturation surface of H2O+CO2 fluids in silicate melts. Chem. Geol. 229, 78–95.

Price, S. E., Russell, J. K., Kopylova, M. G., 2000. Primitive Magma From the Jericho Pipe, N.W.T., Canada: Constraints on Primary Kimberlite Melt Chemistry. J. Petrol. 41, 789–808.

Russell, J. K., 1987. Crystallization and vesiculation of the 1984 eruption of Mauna Loa. J. Geophys. Res. Solid Earth 92, 13731–13743.

Russell, J. K., Porritt, L. A., Hilchie, L., 2013. Kimberlite: Rapid Ascent of Lithospherically Modified Carbonatitic Melts, in: Proc. 10th Int. Kimberl. Conf. Springer India, pp. 195–210.

Russell, J. K., Porritt, L. A., Lavallée, Y., Dingwell, D. B., 2012. Kimberlite ascent by assimilation-fuelled buoyancy. Nature 481, 352–356.

Scott Smith, B. H., 2008. Canadian kimberlites: Geological characteristics relevant to emplacement. J. Volcanol. Geotherm. Res. 174, 9–19.

Seifert, R., Malfait, W. J., Lerch, P., Sanchez-Valle, C., 2013. Partial molar volume and compressibility of dissolved CO2 in glasses with magmatic compositions. Chem. Geol. 358, 119–130.

Shishkina, T. A., Botcharnikov, R. E., Holtz, F., Almeev, R. R., Portnyagin, M. V., 2010. Solubility of H2O- and CO2-bearing fluids in tholeiitic basalts at pressures up to 500 MPa. Chem. Geol. 277, 115–125.

Skinner, E. M. W., Marsh, J. S., 2004. Distinct kimberlite pipe classes with contrasting eruption processes. Lithos 76, 183–200.

Smith, B. H. S., Nowicki, T. E., Russell, J. K., Webb, K. J., Mitchell, R. H., Hetman, C. M., Harder, M., Skinner, E. M. W., Robey, J. A., 2013. Kimberlite Terminology and Classification, in: Proc. 10th Int. Kimberl. Conf. Springer India, pp. 1–17.

Sparks, R. S. J., 2013. Kimberlite volcanism. Annu. Rev. Earth Planet. Sci. 41, 497–528.

Sparks, R. S. J., Baker, L., Brown, R. J., Field, M., Schumacher, J., Stripp, G., Walters, A., 2006. Dynamical constraints on kimberlite volcanism. J. Volcanol. Geotherm. Res. 155, 18–48.

Stripp, G. R., Field, M., Schumacher, J. C., Sparks, R. S. J., Cressey, G., 2006. Post-emplacement serpentinization and related hydrothermal metamorphism in a kimberlite from Venetia, South Africa. J. Metamorph. Geol. 24, 515–534.

Tamic, N., Behrens, H., Holtz, F., 2001. The solubility of H2O and CO2 in rhyolitic melts in equilibrium with a mixed CO2–H2O fluid phase. Chem. Geol. 174, 333–347.

Vetere, F., Botcharnikov, R. E., Holtz, F., Behrens, H., De Rosa, R., 2011. Solubility of H2O and CO2 in shoshonitic melts at 1250 °C and pressures from 50 to 400 MPa: Implications for Campi Flegrei magmatic systems. J. Volcanol. Geotherm. Res. 202, 251–261.

Walter, M. J., Kohn, S. C., Araujo, D., Bulanova, G. P., Smith, C. B., Gaillou, E., Wang, J., Steele, A., Shirey, S. B., 2011. Deep mantle cycling of oceanic crust; evidence from diamonds and their mineral inclusions. Science 334, 54–57.

Woods, A. W., 1995. The dynamics of explosive volcanic eruptions. Rev. Geophys. 33, 495–530.

Zhang, C., Duan, Z., 2009. A model for C–O–H fluid in the Earth's mantle. Geochim. Cosmochim. Acta - GEOCHIM COSMOCHIM ACTA 73, 2089–2102.

FIGURES

Figure 1: Optical microphotograph showing the results from various supra-liquidus, volatile-saturated experimental run producing a pure glass. All samples shown are synthesised in IHPV apparatus.

Figure 2: A. Raman spectra of a kimberlitic glass containing 4.3 wt.% CO_2 and 5.2 wt.% H_2O. The position of the carbonate ion C-O stretching vibration ν_1 is indicated together with the position of Si-O silicate network stretching vibrational signature and water stretching frequency. Raman spectra were measured with a Jobin-Yvon Labram spectrometer (focal distance = 300 mm) equipped with a 2400 grooves/mm CCD detector. Analyses were performed in confocal mode (hole= 500 μm, slit = 100μm) and using a x50 Olympus objective reducing the analysed volume size to a few μm^3. We used an Innova 300-5W Argon ion laser (Coherent©) operating at 514 nm as the light source to produce Raman scattering. The acquisition time was of 10 x 60 sec and acquisition depth was optimised in order to obtain the highest Raman signal. **B**. Infrared spectra of the same glass. The position of the carbonate antisymmetric stretch ν_3 doublet is indicated together with the water stretching frequency. Note that all CO_2 is contained as carbonate, as testified by the absence of CO_2^{mol} at ~2350 cm^{-1} in the infrared spectra. Spectra were collected using a Nicolet 6700 spectrometer attached to a Continuum microscope. We used an IR source with a KBr beam splitter and a liquid nitrogen cooled MCT/A detector. The spectral resolution was set to 4 cm^{-1}, and spectra were accumulated for 128 scans.

Figure 3: Experimentally determined solubility of CO_2 and H_2O in transitional melts (data in table 2).). (**a**) Dissolved H_2O in wt.% vs. fugacity of H_2O for data from this study and from Behrens et al., 2009, Shishkina et al., 2010, Vetere et al., 2011 and Botcharnikov et al., 2006.

Fugacity coefficients for all data were calculated using the model of Zhang and Duan, (2009). Green dotted line shows a water solubility to f_{H2O} power law relationship of equation: $y = 0.0655x^{0.5541}$ ($R^2 = 0.94$) determined by least square regression of data from tholeitic basalt (Shishkina et al., 2010). (**b**) Dissolved CO_2 in wt.% vs. fugacity of CO_2 for data from this study and from Behrens et al., 2009, Shishkina et al., 2010, Vetere et al., 2011 and Moussallam et al., 2014. Data from Moussallam et al., (2014) of similar composition but equilibrated with CO_2 as the sole fluid phase are shown with a black cross overlaid on the symbol. Fugacity coefficients for all data were calculated using the model of Zhang and Duan, (2009). Green dotted line shows least square regression of data from tholeitic basalt (Shishkina et al., 2010). Blue and Red dotted lines shows the predicted CO_2 solubility vs f_{CO2} relationship from the model of Moussallam et al., (2014) for SiO_2 content of 25 and 32 wt.% (on a volatile-free basis) respectively. (**c**) Dissolved CO_2 in wt.% vs. dissolved H_2O in wt.% for a single composition (SiO_2 content of 25 wt.% on a volatile-free basis) equilibrated at 100 (circle symbols) and 350 (square symbols) MPa. Blue dotted lines are second order polynomial fit to the data. Green dotted line shows the CO_2-H_2O relationship for a typical basalt calculated using the model of Iacono-Marziano et al., (2012). The light grey area represent the range of CO_2 and H_2O contents reported for "uncontaminated kimberlite" (database from Kjarsgaard et al., 2009), single analyses are reported as small grey crosses.

Figure 4: **A**. H_2O-CO_2 solubilities calculated for a composition with 25 wt% SiO_2 on a volatile free basis (TA6; Table 1). Black dashed lines are isobaric curves for total pressure of 350 and 100 MPa calculated from the model of Papale et al., (2006), dashed blue lines are fits to the experimental data (circles are from experiments at 100 MPa while squares are from experiments at 350 MPa). **B**. Dissolved CO_2 in wt% vs. partial pressure of CO_2 for our data and those of Moussallam et al., (2014) (shown with a black cross overlaid on the symbol).

Black dashed line shows the solubility modelled used by Sparks et al., (2006) in their kimberlite ascent model. Blue and Red dashed lines shows the predicted CO_2 solubility vs P_{CO2} relationship from the model of Moussallam et al., (2014) for SiO_2 + Al_2O_3 content of 30 and 39 wt.% respectively (on a volatile-free basis).

Figure 5: Left hand panel: CO_2 solubility as a function of pressure for two Kimberlite/Transitional melt compositions with SiO_2 content of 25 and 32 wt.% (on a volatile-free basis) and variable amount of H_2O from 0 to 10 wt.% dissolved at 1500 MPa (equivalent to an initial X_{CO2} at 1500 MPa of 1, 0.7 and 0.5 for the composition with 25 wt.% SiO_2 and of 1, 0.6 and 0.4 for the composition with 32 wt.% SiO_2. Central panel: Evolution of kimberlitic ascent speed during ascent through a 50 km thick crust. The physical model considers the ascent of a kimberlite melt in a self-propagating dyke based on Lister and Kerr, (1991); Sparks et al., (2006) and is described in the text. The light-brown colour part of each plot represents the upper 2.5 km of crust, corresponding to the typical root zone of Kimberlites. Right hand panel shows the evolution of the total volatile content (H_2O + CO_2) in the upper five kilometres of ascent and shows how water-rich kimberlite enter the typical root zone with less dissolved volatiles than water-poor kimberlites. By exsolving volatiles (mainly CO_2) at greater depth water-rich kimberlite ascend through the crust twice as fast as water-free kimberlite.

Figure 6: Left hand panel: evolution of the volume fraction of gas in the upper 5 km for the six scenarios of kimberlite ascent shown in Fig. 5. Vertical dark grey stripe shows the depth at which 70 to 80 vol% of the mixture volume is composed of gas. At this point the bubble foam collapses to form an ash-laden gas (e.g., Woods, 1995). This phase change will

radically change the ascent dynamics as the flow becomes highly turbulent and frictional forces are reduced. Horizontal light grey shaded area shows the typical depth of kimberlite root zones. Right hand panel: Schematic representation of the depth extent of kimberlite pipes produced as a function of melt chemistry. Note that water has the strongest effect on deepening the depth at which large amount of volatile are release, producing pipes with deep root zone (i.e. class 1 kimberlite bodies as found in South Africa).

TABLES

Table 1: Starting oxide and natural rock powder mix compositions. The composition of a natural lamproite from Torre Alfina, Italy, used to prepare the oxide-mix compositions is reported at the top of the table. Notice that the only difference between TA6, TA14 and TA16 oxide mixes is the CO_2 content. TA14 and TA16 mixes were produced using a mix of CaO (preliminary decarbonised for 48h at 1000°C) and $CaCO_3$ oxides while TA6 was produced using $CaCO_3$ as the only added source of calcium.

Table 2: Run conditions, EMP analyses (averaged of 20); total volatile (H_2O +CO_2) content determined by (i) EMPA shortfall, (ii) elemental analyser (Flash) and (iii) gravimetric weight loss (difference between the initial amount of volatile loaded and the amount of volatile in the gas phase measured by weight loss after each capsule was punctured and heated to 140°C); H_2O content determined by elemental analyser (Flash) and CO_2 determined from: (i) EMPA (by subtracting H_2O content to EMPA shortfall) and (ii) Elemental analyser (Flash). Run duration was of 2 hours in all experiments. Partial pressure of water and CO_2 were calculated using the gas phase composition (itself calculated by mass balance between the initial loaded volatile content and the amount of each volatile dissolved in the melt). Partial pressure were

then converted to fugacity's using fugacity coefficients from Zhang and Duan, (2009) for pure water and CO_2 species. Error reported in table S1.

Name	SiO_2	TiO_2	Al_2O_3	FeO	MgO	CaO	Na_2O	K_2O	P_2O_5	CO_2	Total
TA	55.7	1.3	13.1	5.8	9.4	5.5	1.0	7.7	0.5	0.0	100
TA6	16.6	0.2	3.9	0.9	6.9	35.5	0.3	2.3	0.1	33.5	100
TA14	21.2	0.2	4.9	1.1	8.8	45.3	0.4	2.9	0.1	15.1	100
TA16	22.7	0.3	5.3	1.2	9.5	48.4	0.4	3.1	0.1	9.2	100
TA9	23.1	0.3	5.4	1.5	8.3	30.2	0.4	3.2	0.1	27.5	100
On a volatile-free basis:											
TA6	25.0	0.3	5.8	1.3	10.4	53.3	0.4	3.4	0.1	0.0	100
TA14	24.9	0.3	5.8	1.3	10.4	53.3	0.4	3.4	0.1	0.0	100
TA16	25.0	0.3	5.8	1.3	10.4	53.3	0.4	3.4	0.1	0.0	100
TA9	31.9	0.5	7.4	2.1	11.4	41.7	0.6	4.4	0.2	0.0	100

Table 1: Starting oxide and natural rock powder mix compositions used for all experiments. The composition of a natural lamproite from Torre Alfina (TA), Italy, is reported at the top of the table. This composition was mixed with various amounts of synthetic powders of pure oxides and natural dolomite $(Ca,Mg)CO_3$ as to produce the four investigated compositions (TA6, TA14, TA16, TA9). Notice that the only difference between TA6, TA14 and TA16 oxide mixes is the CO_2 content. TA14 and TA16 mixes were produced using a mix of CaO (preliminary decarbonised for 48h at 1000°C) and $CaCO_3$ oxides while TA6 was produced using $CaCO_3$ as the only added source of calcium.

							EMP analyses														
Experiment	Pressure (MPa)	Temperature (°C)	X_{H2O} loaded molar ratio	X_{H2O} gas phase molar ratio	f_{H2O} (bar)	f_{CO2} (bar)	SiO_2	TiO_2	Al_2O_3	FeO	MnO	MgO	CaO	Na_2O	K_2O	P_2O_5	Total	Shortfall	CO_2+H_2O (Flash)	CO_2+H_2O (weight loss)	H_2O (Flash)	CO_2 (EMPA)	CO_2 (Flash)
TA6_1_3	345	1225	0.00	0.00	1	7769	18.87	0.19	2.44	0.75	0.03	7.13	44.05	0.24	2.24	0.06	76.01	23.99	21.1	20.9	1.0	23.0	20.1
TA6_1_2	336	1225	0.17	0.26	941	5489	18.74	0.21	4.15	0.86	0.02	7.29	41.75	0.27	2.03	0.05	75.36	24.64	22.3	24.2	3.3	21.3	19.0
TA6_2_4	343	1185	0.46	0.59	2189	3189	18.65	0.23	4.00	0.92	0.03	8.28	42.55	0.32	2.11	0.11	77.26	22.74	22	20.2	3.4	19.3	18.6
TA14_1_2	350	1185	0.73	0.89	3391	856	20.37	0.18	4.09	1.00	0.04	7.86	44.75	0.23	1.80	0.09	80.42	19.58	16.6	14.9	6.1	13.5	10.5
TA16_1_2	350	1185	0.88	0.97	3685	229	19.39	0.23	4.54	0.96	0.04	7.57	43.54	0.17	1.88	0.09	78.41	21.59	14.6	11.8	7.6	14.0	7.0
TA6_2_1	105	1270	0.00	0.00	1	1296	17.8	0.2	2.4	0.7	0.1	8.1	45.2	0.2	2.5	0.1	77.2	22.8	17.3	18.3	0.8	22.0	16.5
TA6_2_2	102	1225	0.00	0.00	1	1279	20.07	0.23	2.80	0.50	0.04	6.98	47.27	0.35	2.03	0.15	80.49	19.51	18.7	17.5	1.5	18.0	17.2
TA6_2_5	101	1185	0.47	0.49	494	636	19.28	0.20	3.76	0.82	0.04	7.73	44.86	0.25	1.93	0.09	78.95	21.05	16.0	15.2	2.9	18.2	13.1
TA6_2_6	100	1185	0.59	0.69	689	385	20.65	0.23	4.55	0.92	0.05	7.51	44.74	0.30	2.38	0.13	81.46	18.54	16.7	15.7	3.2	15.3	13.5
TA14_1_3	100	1185	0.74	0.82	820	223	21.20	0.23	5.22	0.99	0.06	8.33	45.17	0.15	2.73	0.12	84.19	15.81	11.5	8.4	4.8	11.0	6.7
TA16_1_3	101	1185	0.86	0.91	911	115	21.79	0.26	4.92	1.10	0.08	9.89	43.24	0.38	3.44	0.14	85.25	14.75	9.5	7.3	5.2	9.6	4.3
TA9_1_5	335	1185	0.28	0.10	371	6623	26.27	0.39	5.78	1.55	0.04	9.72	35.79	0.33	3.09	0.17	83.14	16.86	14.2	16.1	2.3	14.5	11.9
TA9_1_7	339	1185	0.75	0.76	2791	1786	25.17	0.36	5.44	1.53	0.10	9.92	35.88	0.32	3.11	0.13	81.95	18.05	12.4	15.1	4.8	13.2	7.6
TA9_1_6	336	1185	0.53	0.55	1996	3343	27.78	0.44	6.61	1.78	0.27	8.57	35.38	0.40	2.94	0.18	84.34	15.66	13.8	13.9	3.8	11.9	10.1
Data from Moussallam et al., (2014), also shown in Fig.3:																							
TA6_1_1	357.2	1225	0.00	0.00	0	8287	18.44	0.2	2.05	0.74	0.03	6.87	45.25	0.3	2.3	0.04	76.22	23.8	23.4	24.4	1.54	22.24	21.84
TA6_1_4	178	1220-1260	0.00	0.00	0	2652	17.97	0.19	2.63	0.81	0.04	6.75	44.8	0.41	2.19	0.04	75.83	24.2	21.3	18.9	1.19	22.98	20.07
TA6_1_6	59.3	1225	0.00	0.00	0	670						*Crystallised*							16.7	12.7	0.84		15.87
TA9_1_1	336.4	1225	0.00	0.00	1	7401	26.07	0.35	5.7	1.49	0.04	8.18	36.87	0.45	3.28	0.09	82.52	17.5	16.5	13.4	1.57	15.91	14.95
TA9_1_2	100.7	1225	0.00	0.00	1	1249	24.5	0.5	4.4	1.9	0	8.1	39.8	0.5	4.2	0.1	84.2	15.8	10.7	11.0	0.59	15.22	10.12

Table 2: Run conditions, EMP analyses (averaged of 20); total volatile (H_2O +CO_2) content determined by (i) EMPA shortfall, (ii) elemental analyser (Flash) and (iii) gravimetric weight loss (difference between the initial amount of volatile loaded and the amount of volatile in the gas phase measured by weight loss after each capsule was punctured and heated to 140°C); H_2O content determined by elemental analyser (Flash) and CO_2 determined from: (i) EMPA (by subtracting H_2O content to EMPA shortfall) and (ii) Elemental analyser (Flash). Run duration was of 2 hours in all experiments. Partial pressure of water and CO_2 were calculated using the gas phase composition (itself calculated by mass balance between the initial loaded volatile content and the amount of each volatile dissolved in the melt). Partial pressure were then converted to fugacity's using fugacity coefficients from Zhang and Duan, (2009) for pure water and CO_2 species. Error reported in table S1.

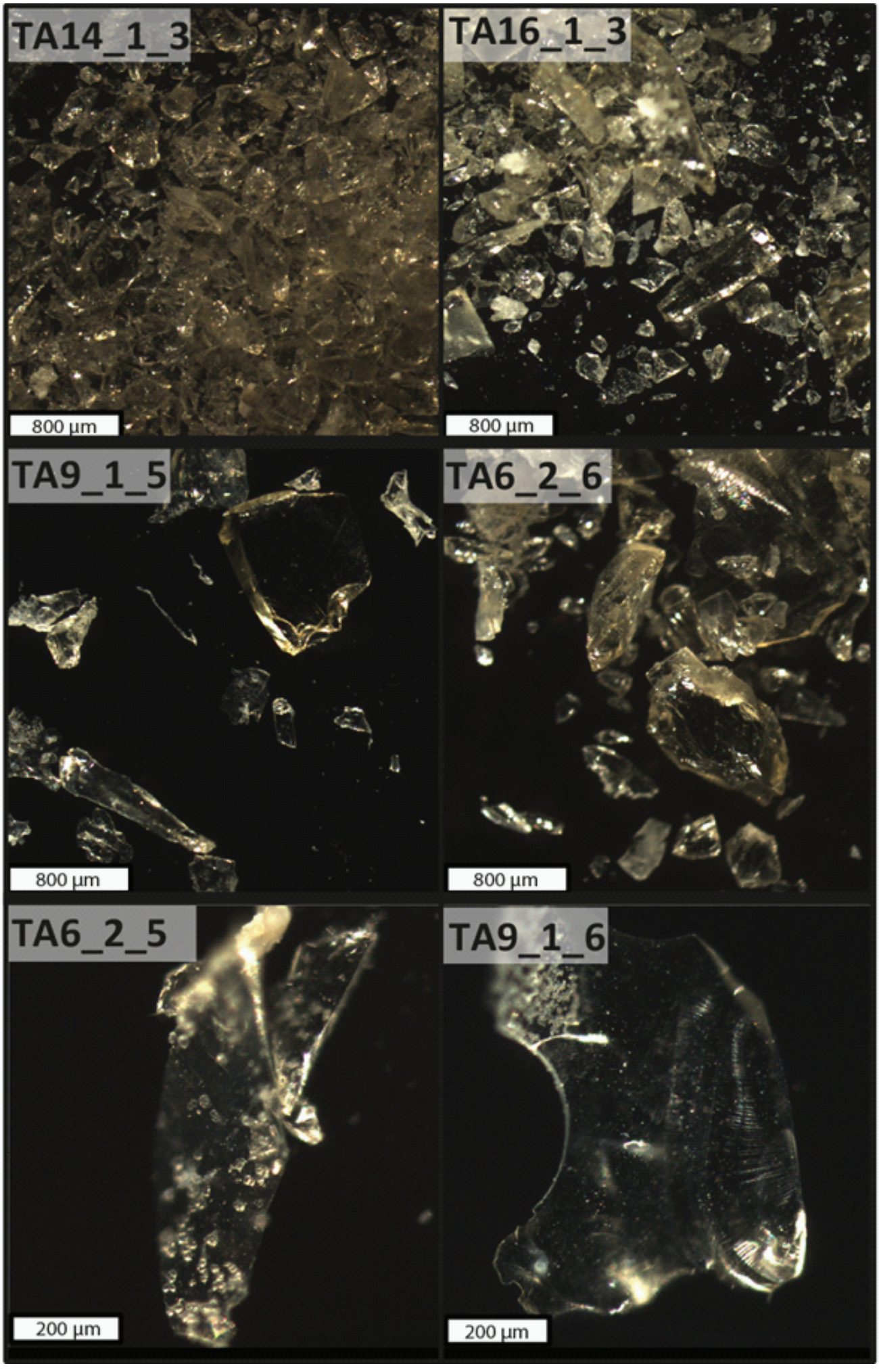

Figure 1, Moussallam et al.

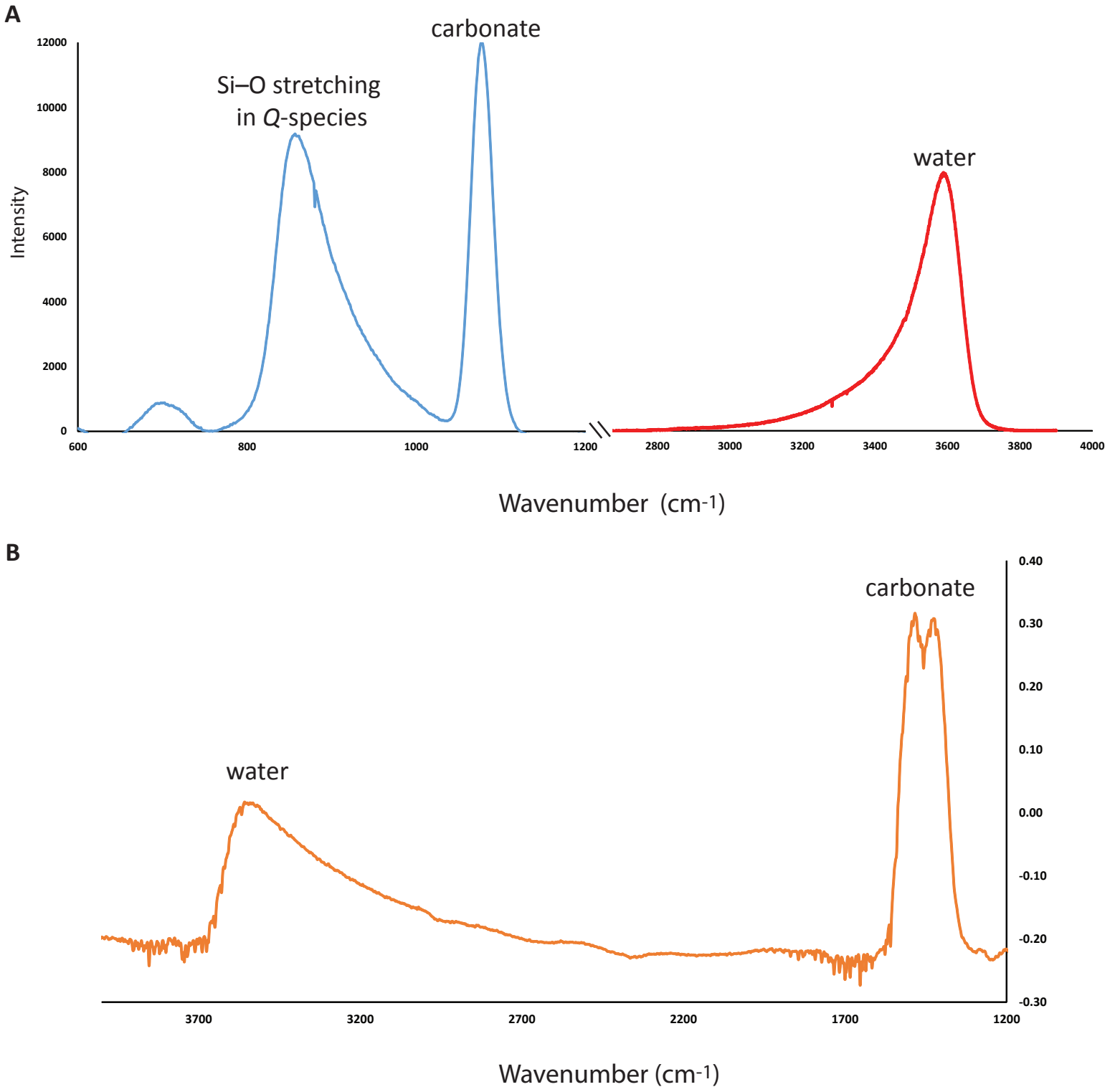

Figure 2, Moussallam et al.

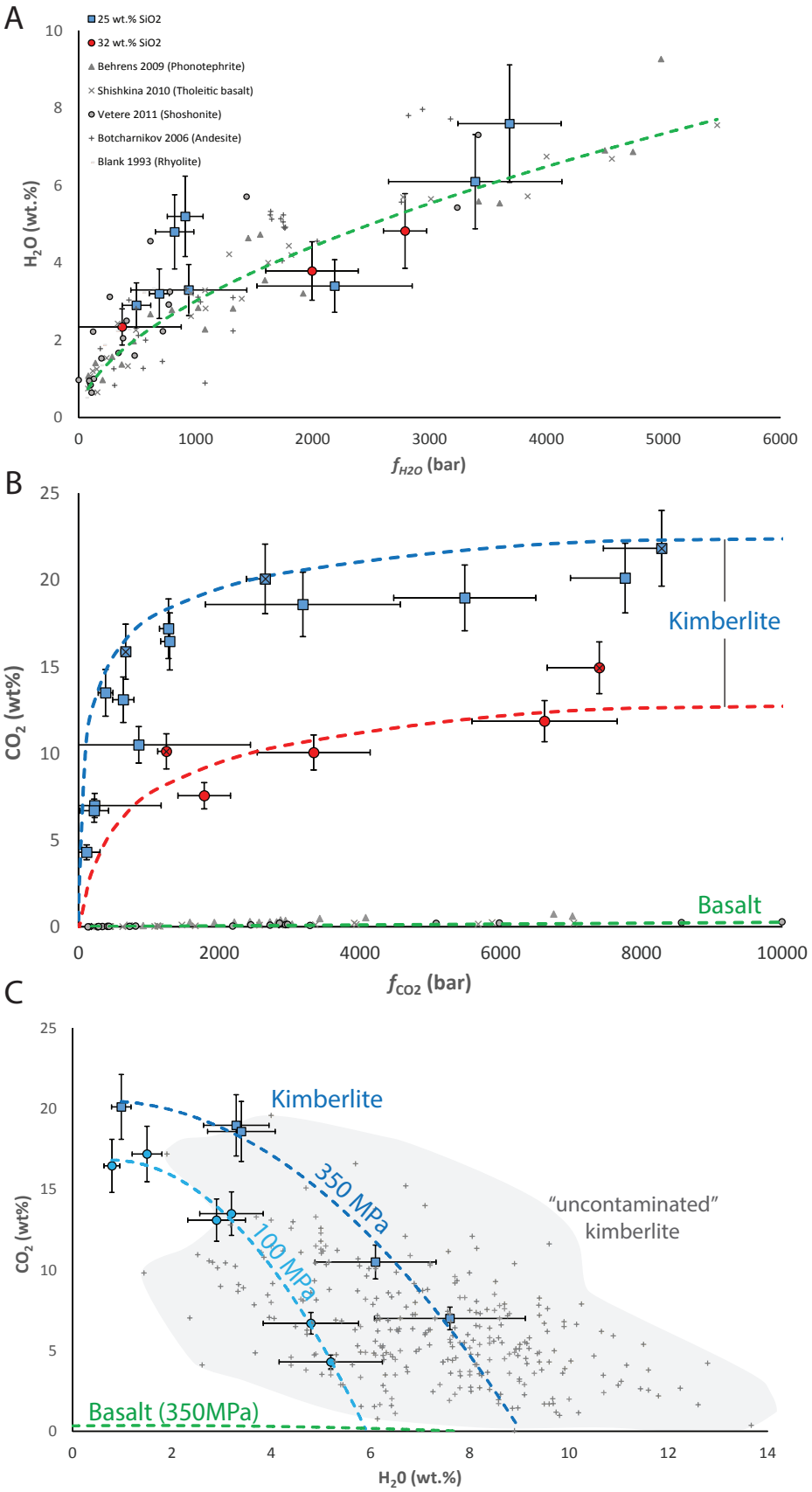

Figure 3, Moussallam et al.

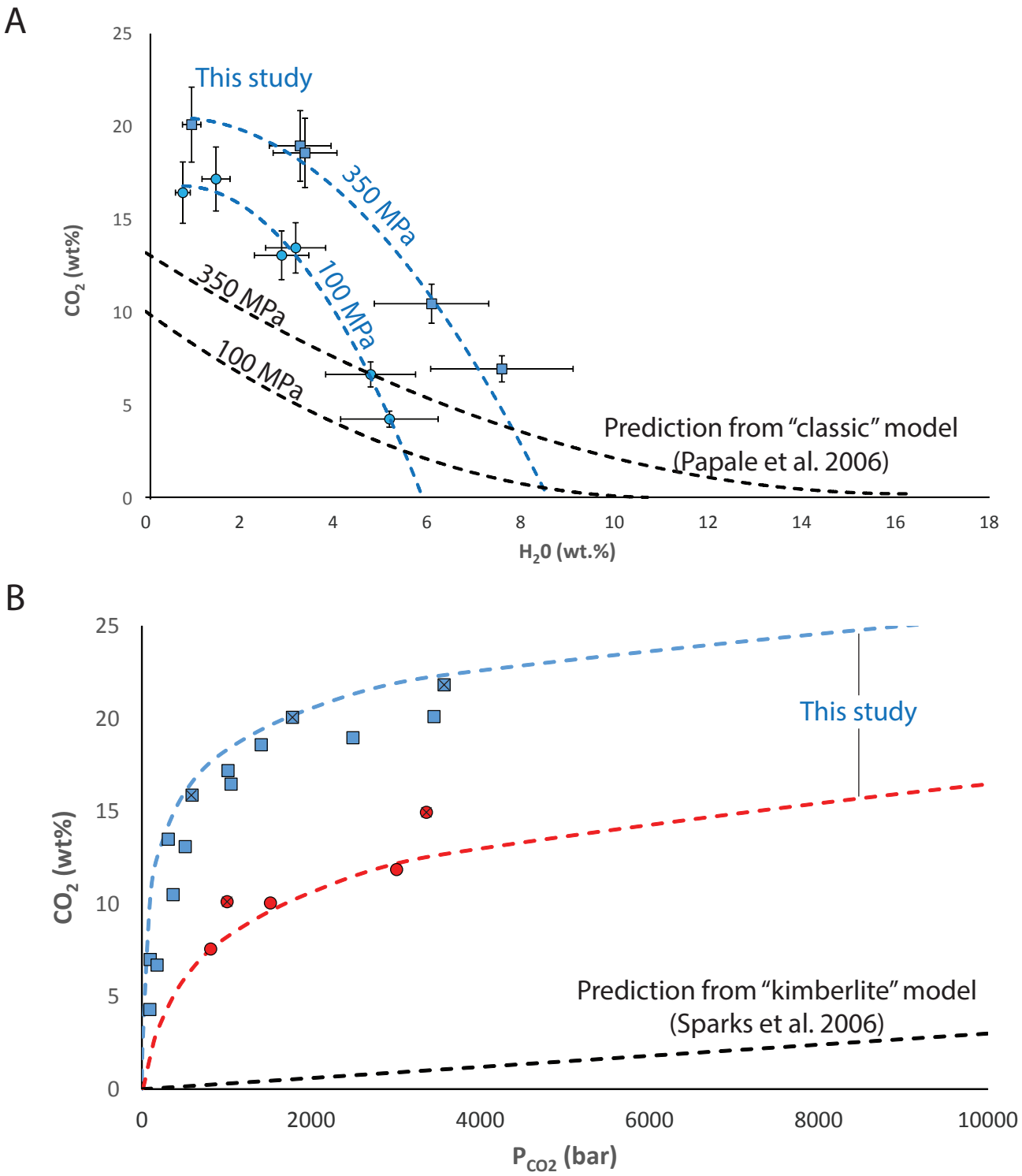

Figure 4, Moussallam et al.

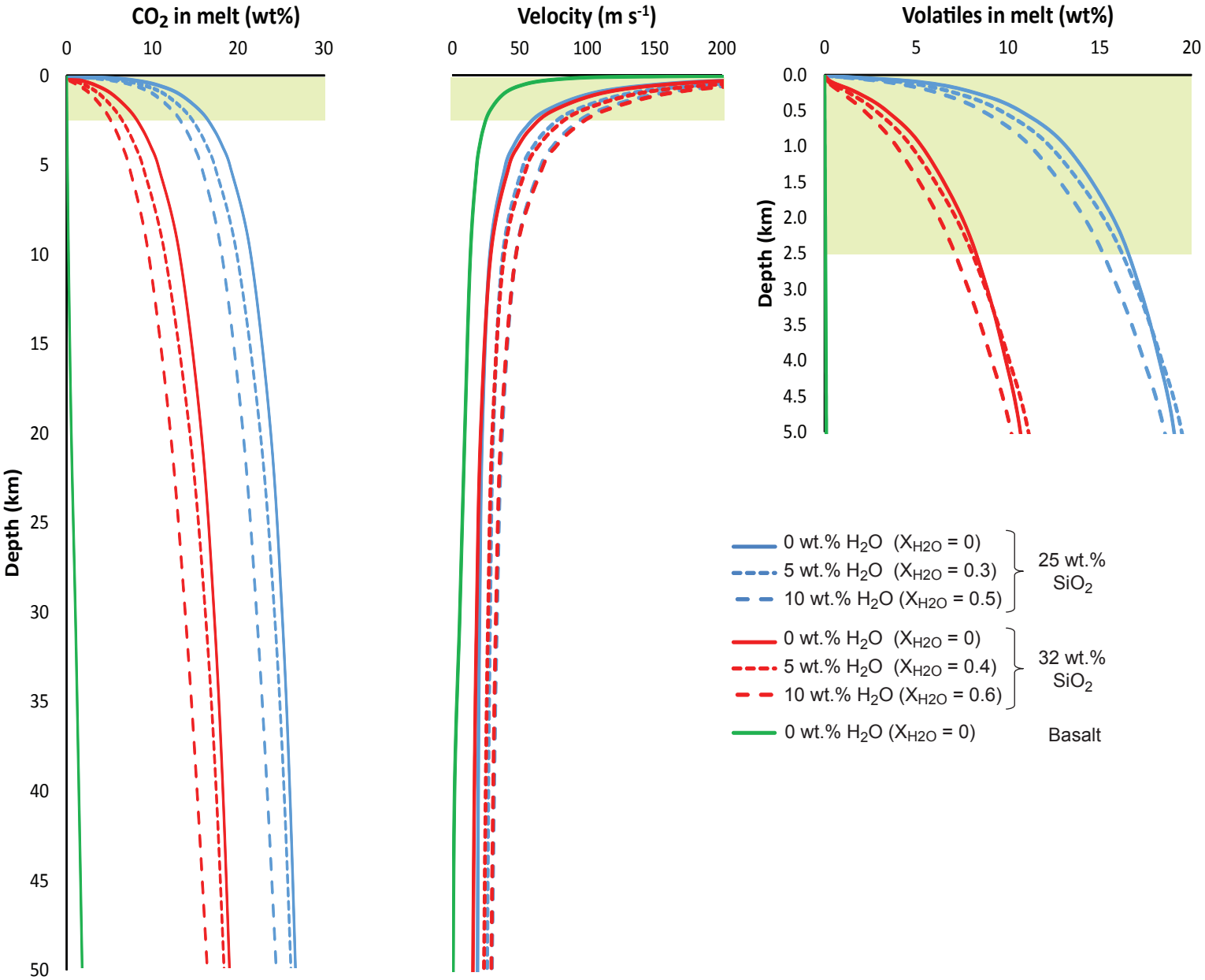

Figure 5, Moussallam et al.

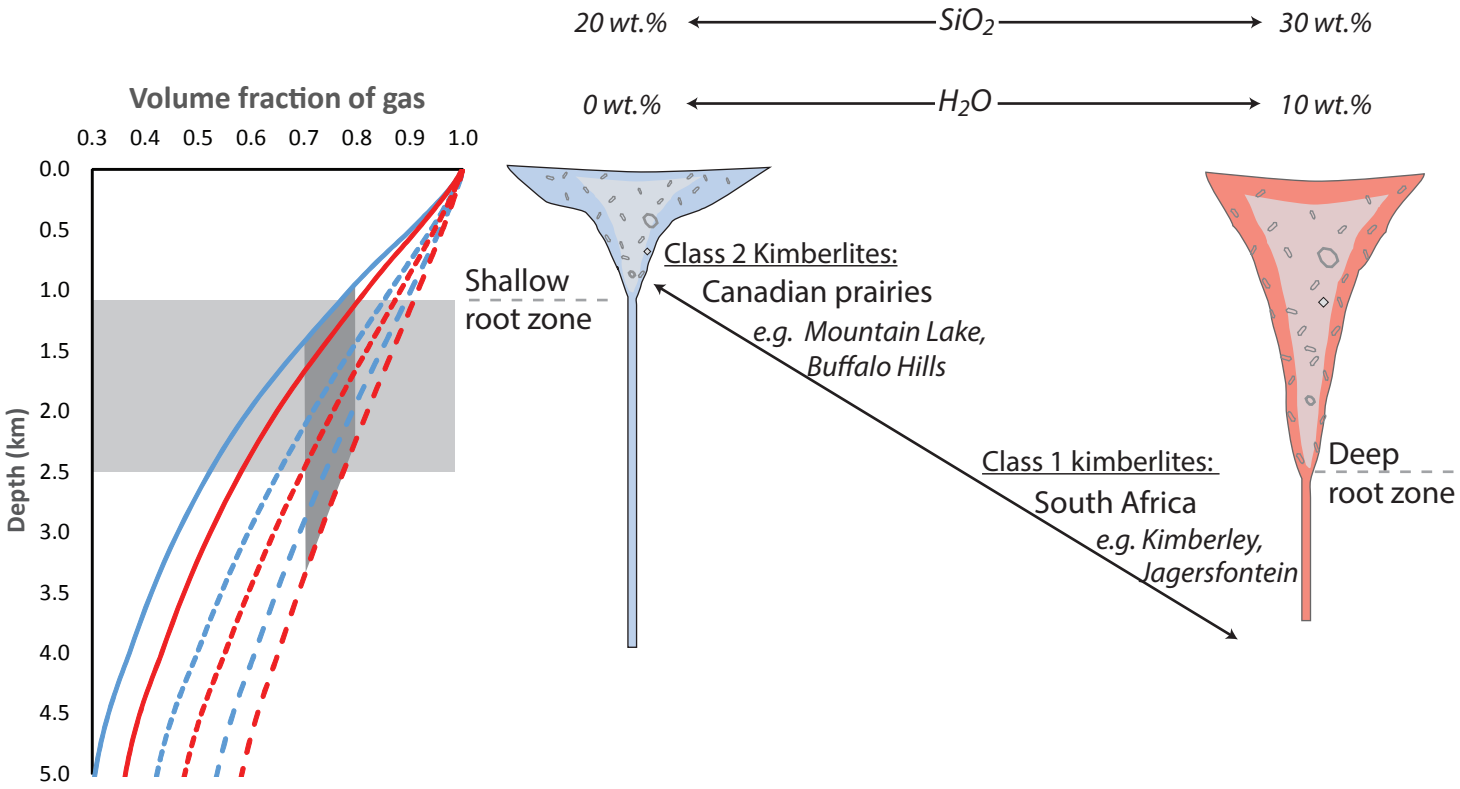

Figure 6, Moussallam et al.